Single-cell RNA sequencing reveals a novel cell type and immunotherapeutic targets in papillary thyroid cancer

Zhengshi Wang[1,2,†], Youlutuziayi Rixiati[3,†], Wenli Jiang[4,†], Chen Ye[5], Caiguo Huang[4], Chuangang Tang[6,*], Zhiqiang Yin[1,2,*], Binghua Jiao[4,*]

[1] Thyroid Center, Shanghai Tenth People's Hospital, Tongji University School of Medicine, Shanghai, P.R.China;

[2] Shanghai Center for Thyroid Diseases, Shanghai, 200072, P.R.China;

[3] Department of Pathology, Soochow University Medical School, Suzhou, 215123, P.R.China;

[4] Department of Biochemistry and Molecular Biology, College of Basic Medical, Navy Medical University, Shanghai, 200433, P.R.China;

[5] Department of Urology, Changhai Hospital, Navy Medical University, Shanghai, 200433, P.R.China;

[6] Department of Thyroid and Breast Surgery, Xuzhou Central Hospital, The Affiliated Xuzhou Hospital of Medical College of Southeast University, Xuzhou, 221009, P.R.China.

[†]They contributed equally to the manuscript.

***Corresponding authors:**

Binghua Jiao, PhD. Department of Biochemistry and Molecular Biology, College of Basic Medical, Navy Medical University, Shanghai, 200433, P.R.China. Tel: +86-13801924888, Email: biojiao@163.com.

Zhiqiang Yin, MD. Shanghai Center for Thyroid Diseases, No. 301, Middle Yanchang Road, Shanghai, P.R.China. Tel.: +86-18917689323, Email: 972683004@qq.com

Chuangang Tang, MD. Department of Thyroid and Breast Surgery, Xuzhou Central Hospital, The Affiliated Xuzhou Hospital of Medical College of Southeast University, Xuzhou, 221009, P.R.China. Tel.: +86-18652230137, Email: tcg3711@163.com.

Abstract

Papillary thyroid cancer (PTC) is the most common thyroid malignancy. Although PTC usually has a favorable prognosis, some aggressive PTC subtypes and lymph node (LN) metastasis contribute to high rates of recurrence and poor clinical outcomes. We analyzed single-cell RNA sequencing (scRNA-seq) data from 15 samples, including primary tumors of PTC, metastatic LNs, and paracancerous tissues. After quality filtering, 28,205 cells were detected. Of these, 13,390 cells originated from 7 tumor tissues, 2,869 cells from 2 metastatic LNs, and 11,945 cells from 6 paracancerous tissues. The increase in the proportion of $CD4^+$ Tregs may be a key factor responsible for the immunosuppressive property of PTC. A novel cell type was identified, named Protective $EGR1^+CD4^+$ T cell, which might be antagonistic to the $CD4^+$ Tregs and inhibit the formation of the immunosuppressive microenvironment and tumor immune evasion. Inhibitory checkpoints TIGIT and CD96 were found to be better targets than PD-1 for immune therapy in PTC patients with LN metastasis. For PTC patients without LN metastasis, however, PD-1, TIGIT, and CD96 could be suitable targets of immunotherapy. These findings would contribute to the further understanding of molecular mechanisms resulting in occurrence and development of PTC, and provide a theoretical rationale for targeted therapy and immunotherapy.

Keywords

papillary thyroid cancer, single-cell RNA sequencing, tumor microenvironment

Introduction

According to the GLOBOCAN database, there were an estimated 586,202 new cases of thyroid cancer worldwide in 2020 [1]. The global incidence was up to 13.1 per 100,000 people, ranking 11th in occurrence rate. The most common pathological type of thyroid cancer is papillary thyroid cancer (PTC), accounting for approximately 85% of all cases [2]. Although PTC usually has a favorable prognosis, some aggressive PTC subtypes (e.g. tall cell variant and Hürthle cell cancer) and lymph node (LN) metastasis contribute to high rates of recurrence and poor clinical outcomes [3, 4]. For PTC patients with a high risk of recurrence, radioiodine treatment could be used to improve their prognosis [5]. However, some PTC patients would develop into radioiodine-refractory PTC, which in turn lead to low survival rate [6, 7]. Therefore, a deeper understanding of molecular and cellular mechanisms of PTC would help in the development of therapeutic strategies.

Currently, efforts to study the tumor progression and metastatic process of thyroid cancer have mainly focused on the analysis of cancer cells using genetic aberrations[8, 9, 10, 11]. However, the tumor progression and metastasis are a complicated biological process, which were not only affected by the characteristic features of cancer cells themselves but also by the tumor microenvironment (TME) [12, 13, 14, 15]. TME refers to a tumor pathology-related environment, comprising stromal cells, extracellular matrix (ECM), and cytokines. A comprehensive analysis of TME in PTC can reveal the key elements involved in the susceptibility of tumor-induced immunological changes, which could be employed to develop new immunotherapy strategies.

Genomic and transcriptomic studies have revealed a huge number of driver mutations, abnormal regulatory programs, and disease subtypes in major human tumors[16, 17, 18, 19]. However, the conventional bulk sequencing frequently adopted in these studies only revealed the overall biological characteristics of each tumor and lacked the ability to capture signatures in intratumoral and intercellular heterogeneity. As opposed to bulk sequencing, the emergence of single-cell RNA sequencing (scRNA-seq) provided a new opportunity to enables characterization of cell populations at the single-cell level, and made it more independent of any previous assumptions about surface markers [20]. scRNA-seq has been applied to investigate cellular properties in various solid tumor types [21]. However, the single-cell atlas of

PTC remains to be fully revealed. Therefore, we analyzed primary PTC tumors, paracancerous tissues, and metastatic LNs using the scRNA-seq-based profiling method to better understand the intratumoral heterogeneity and complexity during the development of PTC.

Results

Single cell atlas and heterogeneity of PTC

A total of 15 samples from seven PTC patients were involved in this study. After quality filtering, 28,205 cells were detected. Of these, 13,390 cells originated from 7 tumor tissues, 2,869 cells from 2 metastatic LNs, and 11,945 cells from 6 paracancerous tissues (Fig. 1a and 1b). Subsequently, we partitioned the cells into 26 clusters, which were further classified into 10 major cell types based on known markers described in previous studies: B cells ($CD19^+$, $MS4A1^+$, $CD38^+$, $CD79A^+$, $CD79B^+$); $CD4^+$ T cells ($CD3D^+$, $CD4^+$); $CD8^+$ T cells ($CD3D^+$, $CD8A^+$); endothelial cells ($CD31^+$, $CD34^{+)}$; epithelial cells ($EPCAM^+$, $KRT18^+$); fibroblasts ($COL1A1^+$); myeloid cells ($CD14^+$, $CD86^+$, $ITGAX^+$, $CD80^+$, $CD83^+$, $ITGAM^+$); naive T cells ($CD3D^+$, $CCR7^+$); natural killer T (NKT) cells ($CD3D^+$, $NKG7^+$); and plasma cells ($CD79A^+$, $SDC1^+$) (Fig. 1c, Supplementary Fig. 1 and 2).

Based on the frequencies of cell types, we detected cellular landscapes in primary tumors, paracancerous tissues, and metastatic LNs, respectively. significant differences were observed in several cell types (Fig. 1d). The immune cells accounted for the major differences between primary tumors and paracancerous tissues, with the frequency of NKT cells and plasma cells increasing, and $CD4^+$ T cells and B cells decreasing in the primary tumors ($P<0.05$). The most striking changes between metastatic LNs and primary tumors were observed in $CD8^+$ T cells. At the cluster level, there were also significant differences within the same cell types. As exemplified by myeloid cells, we observed an increase in the frequency of cluster 21 and a decrease in the proportion of cluster 25 in metastatic LNs compared with primary tumors and paracancerous tissues. These results demonstrated that the disease progression might also be somehow associated with evolutionary immune cells, reflecting the existence of heterogeneity among samples and cell populations.

To conduct the interaction network of tumor microenvironment in PTC, CellphoneDB was used to calculate potential ligand-receptor pairs in cells. And Cytoscape was performed to visualize the cell interaction. We found that myeloid cells and T cell-related cells possessed more interaction pairs with other cells than

119 others (Fig. 1e), showing the dominant roles of myeloid cells and T cells.

120 **Identification of malignant cells in epithelial cells**

121 To distinguish malignant from non-malignant cells within the epithelial cells,
122 CopyKAT was performed to identify PTC genome alterations. Despite the
123 heterogeneity, almost all malignant cells possessed deletions from chromosomes 16
124 and 19 and amplifications in chromosomes 13 (Fig. 2a and 2b). We distinguished
125 1,679 non-malignant cells and 450 cells were identified as malignant cells. Very few
126 malignant cells were also found in paracancerous tissues (Fig. 2b). In order to support
127 the identification results of the malignant cells, pseudotime trajectory analysis was
128 performed. The results showed that malignant cells were present at the end of the
129 differentiation trajectory (Fig. 2c).

130 To screen for key regulons in malignant cells, we conducted SCENIC analysis
131 and identified motifs ATF3 and BHLHE40 that were highly activated in malignant
132 cells (Fig. 2d). In a previous study, ATF3 was found to enhance breast cancer
133 metastasis [36]. At the same time, decreased activity was found in CREM and ETS1. In
134 TCGA THCA cohort, a high level of CREM and ETS1 was significantly related to a
135 good prognosis, and BHLHE40 is highly expressed in patients with LN metastasis
136 compared with patients without LN metastasis (Fig. 2e and 2f). These results provide
137 potential targets for suppressing cells to possess malignant characteristics.

138 We further characterized the functions of differential genes between metastatic
139 LNs and primary tumors by comparing pathway activities. Pathways involved in
140 cellular component assembly, protein-containing complex assembly, and regulation of
141 microtubule motor activity were relatively upregulated in LN-derived malignant cells
142 (Fig. 2g). The results showed that malignant cells in metastatic LNs have stronger cell
143 proliferative and invasive abilities.

144 **Identification of a novel T cell type**

145 Reclustering of T cells identified 10 subclusters: $CD4^+$ Tregs, Cytotoxic $CD8^+$ T
146 cells, Exhausted $CD4^+$ T cells, Follicular helper (Tfh) T cels, Naïve $CD4^+$ T cells,
147 Naïve T cells; NKT cells, Pre-exhausted $CD8^+$ T cells, Proliferating $CD8^+$ T cells, and
148 Protective $EGR1^+CD4^+$ T cells (Fig. 3a and 3b). In addition to the markers used above,
149 we also found some other makers that can be used for cell population identification.
150 For example, TYMS can be used for Pre-exhausted $CD8^+$ T cells identification, and
151 RTKN2 can be used for Pre-exhausted $CD4^+$ Tregs identification (Fig. 3c,
152 Supplementary Fig. 3). Notably, a novel cell type was identified, which was totally

different from preconceived cellular definitions. The novel cell type specifically highly expressed EGR1, and we named it as Protective $EGR1^+CD4^+$T cells. The mRNA expression level and protein level of EGR1 were significantly decreased in tumor tissues compared with normal tissues (Fig. 3d). Survival analysis showed that patients with high EGR1 levels had a better prognosis than those with low EGR1 levels (Fig. 3e). Through cell frequency analysis, we found an interesting phenomenon that the proportion of $CD4^+$ Tregs tended to increase with PTC disease progression and Protective $EGR1^+CD4^+$ T cells exhibited a quite opposite trend (Fig. 3f). The results were validated with TCGA data calculated using Cibersortx (Fig. 3g) and further validated by the changes of marker gene expression levels in the TCGA THCA cohort (Supplementary Fig. 4a). These findings indicated that both of $CD4^+$ Tregs and Protective $EGR1^+CD4^+$ T cells may have an important impact on disease progression, and our newly identified cell type (Protective $EGR1^+CD4^+$T cells) may be antagonistic to the $CD4^+$ Tregs.

We further characterized the functions of $CD4^+$ Tregs and Protective $EGR1^+CD4^+$ T cells by comparing pathway activities. In the primary tumors, $CD4^+$ Tregs and Protective $EGR1^+CD4^+$ T cells exhibited vastly different signaling pathways. $CD4^+$ Tregs were related to epithelial-mesenchymal transition (EMT) and hypoxia, whereas G2M checkpoint and KRAS signaling pathway were significantly down-regulated in Protective $EGR1^+CD4^+$ T cells (Fig. 4a). In the metastatic LNs, mitotic spindle and oxidative phosphorylation were also down-regulated in Protective $EGR1^+CD4^+$ T cells (Supplementary Fig. 4b). To screen for key genes related to tumorigenesis and tumor development in $CD4^+$ Tregs and Protective $EGR1^+CD4^+$ T cells, we conducted SCENIC analysis and identified essential motifs in $CD4^+$ Tregs and Protective $EGR1^+CD4^+$ T cells. FOSL2, ATF3, REL, and HES1 were $CD4^+$ Tregs-specific motifs. BCLAF1 and ETS1 motifs were highly activated in Protective $EGR1^+CD4^+$ T cells (Fig. 4b). These results provided potential targets for inhibiting or reversing the formation of the immunosuppressive microenvironment.

The DEGs derived from Protective $EGR1^+CD4^+$ T cells were identified, including 31 up-regulated mRNAs and 50 down-regulated mRNAs in primary tumors compared with paracancerous tissues (Supplementary Fig. 4c). The DEGs derived from $CD4^+$ Tregs were also identified (Supplementary Fig. 4d). Subsequently, we examined the immune checkpoints in the cell clusters (Fig. 4c and 4d). Notably, we found that TIGIT, an inhibitory checkpoint, was upregulated in Exhausted $CD4^+$ T

cells and CD96 was upregulated in Pre-exhausted $CD8^+$ T cells in metastatic LNs. In tumor tissues, PDCD1 (PD-1) and TIGHT were significantly upregulated in Exhausted $CD4^+$ T cells, and CD96 was significantly upregulated in Pre-exhausted $CD8^+$ T cells. Since TIGIT, CD96, and PDCD1 (PD-1) are markers of T cell exhaustion, these data indicated that Exhausted $CD4^+$ T cells and Pre-exhausted $CD8^+$ T cells were exhausted in the tumor microenvironment, which was consistent with our previous cell population classification results.

Neutrophils cells are extremely reduced in tumor

For exploring the heterogeneity among myeloid cells, 1607 myeloid cells were clustered into 5 cell subtypes based on known markers described in previous studies: macrophages, dendritic cells, monocytes, neutrophils, and myeloid-derived suppressor cells (Fig. 5a and 5b). Through cell frequency analysis, a marked decrease of neutrophils was observed in tumors while the proportion of macrophages increased continuously as the disease progressed (Fig. 5c). The trend was consistent with TCGA data calculated by cibersortx (Fig. 5d). Survival analysis showed that disease-free survival (DFS) of patients with low-level dendritic cell was longer than that of the high-level group in the TCGA cohort (Fig. 5e). Similar results were observed in macrophages (Supplementary Fig. 5a). However, low-level neutrophil was observed to be associated with better prognosis (Supplementary Fig. 5b). These results suggested that macrophages, dendritic cells, and neutrophils are more relevant to the development of PTC.

We further characterized the functions of myeloid cell subtypes by comparing pathway activities. Compared with paracancerous tissues, the cancer hallmark-related pathways were relatively enriched in myeloid-derived suppressor cells from tumors, whereas they were generally down-regulated in neutrophils from tumors (Fig. 6a). These were consistent with the changes in cell proportions we observed earlier (Fig. 5c). Compared with tumor tissues, however, some cancer hallmark-related pathways (i.e. mTORC1 signaling and E2F targets) were down-regulated in myeloid-derived suppressor cells from metastatic LNs (Fig. 6b). The results indicated that myeloid-derived suppressor cells were involved in cancer cell proliferation, but not in tumor metastasis.

In order to screen for key genes related to tumor occurrence and development in myeloid cells, we conducted SCENIC analysis and identified essential motifs in myeloid cells subtypes. Similar to the results of pathway analysis, the overall

regulatory factors in neutrophils were also inconsistent with the other cell types (Fig. 6c). We recognized that the decreased activity of a lot of motifs (i.e. YY1 and IRF5) and activation of the STAT3, ZNF143, and HCFC1 motifs led to the reduction of neutrophils.

As shown in Fig. 6d, cells from myeloid cell-derived cluster 8 uniquely expressed the M1 macrophages marker CCL5, whereas M2 macrophages markers including CTSB/CTSD/FN1 were relatively highly expressed in cluster 0. The proportion of cluster 0 was high in tumors and LNs, although the difference has not reached a significant level (Fig. 5c). All of this evidence certified that cluster 0 represented an M2-like tumor-associated macrophages (TAM) cluster, the increase of which may be related to disease progression. Cluster 9 highly expressed the cytokines CCL17/CCL19/CCL22. These cytokines could bind to CCR4, a marker on the cell membrane of $CD4^+$ Tregs, and showed strong chemotaxis to $CD4^+$ Tregs [37, 38]. It corroborated with our above results that the increasing trend of $CD4^+$ Tregs with disease progression was coincident with that of myeloid cell-derived cluster 9 (Fig. 3f and 5c). The findings indicated that the dendritic cells (cluster 9) could recruit $CD4^+$ Tregs into the tumor regions, thereby acting as an immunosuppressive effect.

Discussion

At present, the study of molecular mechanisms underlying the occurrence and development of PTC mainly focused on the genetical alteration based on bulk sequencing data. We profiled integrated and heterologous transcriptional landscapes of PTC using single-cell sequencing methods, including cancer cells and TME of primary tumors and metastatic lesions. Through sequencing 28,205 cells, we found that the majority of cell clusters possessed strong heterogeneities. Tumor heterogeneity exists in various malignancies and remains not only between tumors but also within a single tumor [39], which is considered as a cause of chemoresistance of cancer. In-depth knowledge of tumor heterogeneity of PTC will make molecular testing more reliable and accurate prior to surgery (whether to undergo the surgery or close follow-up only), and benefit to stratify the recurrence risk and personalized precision treatment (thyroidectomy or total thyroidectomy or plus radioiodine treatment). On the other hand, TME on disease progression and metastasis has also been confirmed in numerous diseases[40, 41]. Investigations of TME-related cellular and molecular events will provide a theoretical rationale for drug discovery and development, especially for targeted therapy and immunotherapy.

In addition to previously described cell types, we discovered a novel cell subpopulation, named Protective $EGR1^{+}CD4^{+}$T cells. EGR1 is a transcription factor primarily mediate cellular functions (i.e. cell growth, cancer progress and apoptosis) via the RAS/RAF/MEK/ERK signaling pathway [42], which was a hallmark of PTC [43]. It has also been previously reported that p53 could bind to EGR1 promoter and subsequently resulted in efficient apoptosis [44]. EGR1 was usually considered a tumor suppressor in many human malignancies including PTC [45, 46, 47, 48]. By comparing the proportion of cells from different tissues and pathway enrichment analyzing, we found that KRAS signaling pathway (part of RAS/RAF/MEK/ERK signaling pathway) was significantly down-regulated in Protective $EGR1^{+}CD4^{+}$ T cells. It indicated that Protective $EGR1^{+}CD4^{+}$T cells might inhibit the formation of the immunosuppressive microenvironment and tumor immune evasion via RAS/RAF/MEK/ERK signaling pathway, thereby restraining tumor growth. Therefore, EGR1 might represent a potential therapeutic target for PTC.

$CD4^{+}$ Tregs, were overall considered to disrupt anti-tumor immunity and then help tumor cells to achieve immune evasion, leading to the tumor growth and metastasis [49]. Our results also showed that $CD4^{+}$ Tregs had the greatest positive correlation with the process of EMT, which matched those reported in other studies of PTC patients [50]. Using pathway enrichment analysis, we found that relevant pathways associated with $CD4^{+}$ Tregs and Protective EGR1+CD4+T cells were almost the opposite. The proportion of $CD4^{+}$ Tregs among three samples increased in the disease progression order (paracancerous tissues < tumors < LNs) while the proportion of Protective $EGR1^{+}CD4^{+}$T cells decreased sequentially. This strongly suggested that $CD4^{+}$ Tregs and Protective $EGR1^{+}CD4^{+}$T cells might act antagonistically to each other.

Immunotherapy is an emerging method for cancer treatment and promising results have been obtained in both hematologic and solid tumors [51, 52]. T cell exhaustion is a critical mechanism of immune evasion. Blockade the PD1/PDL1 interaction to reverse T cell exhaustion is considered a milestone achievement in the field of immunotherapy [53, 54, 55]. Our results showed that PDCD1 (PD-1), TIGIT, and CD96 could be suitable targets of immunotherapy in PTC patients without LN metastasis since they were upregulated in tumor tissues. However, the expression levels of TIGIT and CD96 were much higher than that of PDCD1 (PD-1) in LN-derived exhausted T cell types (Exhausted $CD4^{+}$ T cells and Pre-exhausted $CD8^{+}$

T cells). Therefore, TIGIT and CD96 might be better therapeutic targets for immunotherapy in PTC patients with LN metastasis than PDCD1 (PD-1). Jill et al. [56] investigated the $CD4^+$ and $CD8^+$ T cell exhaustion in PTC patients with LN metastasis using flow cytometry, and found that CD8+ T cell exhaustion was incomplete. This was most likely because TIGHT and CD96 were not included into analysis in their study, both of which were very important inhibitory immune checkpoints. However, their findings supported our conclusions to some extent that PDCD1 (PD-1) was not a suitable molecular target for the treatment of PTC with LN metastasis.

We initially applied a commonly used method inferCNV for the identification of malignant cells [57], which was shown to be unable to identify efficiently malignant tumor cells from epithelial cells in this study. Thus, we adapted an integrative Bayesian segmentation approach called CopyKAT and solved the conundrum successfully [35]. As a result, more than half of tumor-derived epithelial cells were non-malignant cells, which might well explain the reason for the indolent clinical behavior of PTC. Additionally, there were also a very small number of malignant epithelial cells in paracancerous tissues, possibly due to the presence of the pre-tumor microenvironment in paracancerous tissues. There were several possible reasons. First, the pre-metastatic niche, a favorable microenvironment to tumor metastasis, formed in paracancerous tissues [58], and in turn lead to intra-thyroid metastasis. The concept of intra-thyroid metastasis of thyroid cancer has not been described yet. The reason is possibly caused by the small size of the thyroid gland itself and the narrow lumen of artery/vein nourishing the thyroid gland. As is well-known, liver cancer tends to present with intrahepatic metastatic disease, mainly due to the large diameter of the portal vein and hepatic artery. Second, multifocal PTC has already existed within the thyroid gland, whereas the extremely tiny lesion cannot be detected under microscopic examination. Based on the two points above, thyroidectomy is necessary to be performed for patients with PTC at least to ensure a total removal of potential lesions. Third, CopyKAT is not able to discriminate malignant cells from non-malignant cells with hundred percent accuracy.

In summary, we initially investigated the single-cell level heterogeneity of primary PTC tumors and metastatic lesions. A novel cell type, named Protective EGR1+CD4+T cells, was identified, which might inhibit the formation of the immunosuppressive microenvironment and tumor immune evasion. TIGIT and CD96 might be better therapeutic targets for immunotherapy in PTC patients with LN

metastasis than PDCD1 (PD-1). These findings would contribute to the further understanding of molecular mechanisms resulting in occurrence and development of PTC, and provide a theoretical rationale for targeted therapy and immunotherapy.

Methods

Sample collection and clinical information

Seven patients diagnosed with PTC were obtained from Shanghai Tenth People's Hospital. A total of 15 tissue samples (7 tumor tissues, 6 paracancerous tissues, and 2 metastatic LNs) were obtained from 7 PTC patients. Written informed consent was obtained from all patients in the present study. Histological diagnosis of all the samples was confirmed by the pathology department.

Tissue digestion and single-cell suspension preparation

Cells of each sample were firstly stained with two fluorescent dye, Calcein AM (Thermo Fisher Scientific Cat. No. C1430) and Draq7 (Cat. No. 564904), for precisely determination of cell concentration and viability via BD Rhapsody™ Scanner before single-cell multiplexing labeling. The cells of each sample were sequentially labeled with BD Human Single-Cell Multiplexing Kit (Cat. No. 633781) which utilizing an innovative antibody-oligo technology [22] mainly to provide higher sample throughput and eliminate batch effect for single-cell library preparation and sequencing. A set of 12 antibodies in this kit recognize the same universally expressed cell-surface antigen of human cells. Each antibody is conjugated with a Sample Tag, a unique 45-nucleotide barcode sequence. Briefly, cells from each sample were labeled by antibodies with different sample tags respectively and washed twice with BD Pharmingen™ Stain Buffer (FBS) (Cat. No. 554656) before pooling all samples together. BD Rhapsody Express system[23]based on Fan et al. was utilized for single-cell transcriptome capturation. Pooled samples were then loaded in one BD Rhapsody™ Cartridge that was primed and treated strictly following the manufacturer's protocol (BD Biosciences). Cell Capture Beads (BD Biosciences) were then loaded excessively onto the cartridge to ensure that nearly every micro-well contains one bead, and excess beads were washed away from the cartridge. Viable cells with beads captured in wells were detected in BD Rhapsody™. Then cells were lysed, Cell Capture Beads were retrieved and washed before performing reverse transcription and treatment with exonuclease I.

Library construction and sequencing

Transcriptome and SampleTag information of single-cells was obtained through BD Rhapsody System. Microbeads-captured single cell transcriptome and SampleTag sequences were generated into the cDNA library and SampleTag library separately

containing cell labels and unique molecular identifiers (UMI) information. Briefly, double-strand cDNA was firstly generated from microbeads-captured single-cell transcriptome through several steps including reverse transcription, second-strand synthesis, end preparation, adapter ligation, and whole transcriptome amplification. Then final cDNA library was generated from double-strand full-length cDNA by random priming amplification with BD Rhapsody cDNA Kit (BD Biosciences, Catalog No.: 633773) and BD Rhapsody Targeted mRNA & AbSeq Amplification Kit (BD Biosciences, Catalog No.: 633774). On the other hand, the SampleTag library was generated from microbeads-captured single-cell SampleTag sequences through several steps including reverse transcription, nest PCR, and final index PCR. Libraries were sequenced on the NovaSeq platform (Illumina).

Raw data preprocessing and quality control

Raw sequencing reads of the cDNA library and SampleTag library were processed through the BD Rhapsody Whole Transcriptome Assay Analysis Pipeline (Early access), which included filtering by reads quality, annotating reads, annotating molecules, determining putative cells, and generating single-cell expression matrix. Briefly, read pairs with low sequencing quality were firstly removed. The quality-filtered R1 reads were analyzed to identify the sequence of cell labels, UMI sequence, and poly-dT tail sequence, meanwhile the quality-filtered R2 reads were mapped to Genome Reference Consortium Human Build 38 (GRCh38) using STAR (version 2.5.2b) in the reads annotation step. Further adjustment was performed with the recursive substitution error correction (RSEC) and distribution-based error correction (DBEC) algorithms to remove artifact molecules due to amplification bias in the molecules annotation step. Putative cells were distinguished from background noise with second derivative analysis in the putative cell determination step. Finally, putative cells information was combined with molecules adjusted by the recursive substitution error correction and distribution-based error correction algorithms to generate a single-cell expression matrix. The pipeline also determined the sample origin of every single cells via the sample determination algorithm according to the sequencing reads of the SampleTag library. The algorithm classified all putative single cell into three categories: Multiplet, two or more SampleTag exceed their minimum thresholds, indicating more than one actual cell in one micro-well. Undetermined, not enough SampleTag reads for the sample origin. SampleTag01-12, only one SampleTag exceed their minimum thresholds. . Among all the output files, Matrix for

UMI counts per cell corrected by DBEC and SampleTag annotation result were used for downstream clustering analysis.

Dimension reduction and clustering

The R package Seurat [23] was utilized for subsequent analysis. Raw gene expression matrices from the cartridge were read into R (version 3.6.0) and converted to Seurat objects. Cells label as “Undetermined” and “Multiple” were excluded in the following analysis. The gene expression matrix was then normalized to the total cellular UMI count. Top 2000 features were selected as highly variable genes for further clustering analysis. In order to reduce dimensionality, PCA was performed based on the highly variable genes after scaling the data with respect to UMI counts. On top of that, the first 9 principal components were chosen for downstream clustering based on the heatmap of principle components, and the elbow plot of principle components to further reduce dimensionality using the UMAP algorithm. The transcriptional markers of each cluster were calculated using the FindAllMarkers function with theMAST package to run the DE testing under the following criteria: log2 fold change > 0.1; $p < 0.05$; min. percentage > 0.25. Top 500 markers of each cluster were then selected to perform a heatmap plot.

Cell annotation and cell type identification

Cell populations were matched to cell types based on the expression of known marker genes and previously identified expression signatures [23, 24, 25, 26, 27, 28].

Comparison of cell clusters and cell type proportion

The change in the fraction of the different cell types was separately computed for each sample across all clusters, as the fraction of cell in each cluster, out of the total number of cells [29]. To assess a statistically significant difference in a fraction of a specific cell type, we performed paired t-test.

Significantly dysregulated genes identification

We identified differentially expressed genes (DEGs) based on analysis of the MAST package using the R. The threshold of DEGs was set as: 1)P-value of F test < 0.05; 2) $|FC| \geq 1.5$.

External data validation with TCGA datasets

CIBERSORTx was used to detect the abundance of cell types identified in the present work in bulk RNA-seq data [30]. After calculated the relative abundance of each cell type, we divided the patients into two groups: high 50% and low 50%. Subsequently, Kaplan-Meier analysis was performed using ggsurvplot function of the R package

'survminer'. Whether the occurrence of cell types in the different subgroups showed significant differences was evaluated by Wilcoxon test.

Functional annotation and enrichment

GO enrichment and KEGG enrichment of DEGs were performed using Fisher exact test with Benjamini-Hochberg multiple testing adjustment. The results were visualized using R package. Gene set variation analysis (GSVA) [31] was performed using 50 hallmark-related gene sets, as described in the GSVA package.

Identification of hub regulons with SENIC

In order to investigate the gene regulatory network of different sample groups, we utilized SCENIC [32] using the R.

Cell-cell communication analysis based on ligand-receptor pairs

Cell-cell communication at the molecular level was analyzed with CellPhoneDB [33].

Cell trajectory analysis with Monocle

In order to reveal the development of malignant cells, we employed Monocle 2, an R package designed for single cell trajectories [34]. After obtaining the differentially expressed genes through differential Gene Test function, the trajectories were visualized as 2D tSNE plots.

Drug-target analysis with TCMID database

After obtaining the differentially expressed genes, we obtain the targeted relationship between drugs and genes from the TCMID database (http://www.megabionet.org/tcmid).

CNV Estimation

CopyKAT [35] (Copynumber Karyotyping of Tumors), a R package was performed to separate tumor cells from normal cells using high-throughput sc-RNAseq data. Cells with extensive genome-wide copy number aberrations (aneuploidy) are considered as tumor cells, whereas stromal normal cells and immune cells often have 2N diploid or near-diploid copy number profiles.

Statistical analysis

Box plots were drawn with the R base package. Hence, the boxes span from the 25th to the 75th percentiles. Violin plots were generated by the ggplot2 R package. Unpaired two-tailed t-tests was used to compare the difference between two groups. While One-way analysis of variance (ANOVA) was used for multiple group comparisons.

Data availability

The cancer genome atlas (TCGA) thyroid cancer (THCA) cohort were downloaded from UCSC XENA (http://xena.ucsc.edu/).

References

1. Sung H, *et al.* Global cancer statistics 2020: GLOBOCAN estimates of incidence and mortality worldwide for 36 cancers in 185 countries. (2021).

2. Fagin JA, Wells SA, Jr. Biologic and Clinical Perspectives on Thyroid Cancer. *N Engl J Med* **375**, 1054-1067 (2016).

3. Yu J, *et al.* Lymph node metastasis prediction of papillary thyroid carcinoma based on transfer learning radiomics. *Nat Commun* **11**, 4807 (2020).

4. Cohen EE, *et al.* Axitinib is an active treatment for all histologic subtypes of advanced thyroid cancer: results from a phase II study. *J Clin Oncol* **26**, 4708-4713 (2008).

5. Jiao C, *et al.* REGgamma ablation impedes dedifferentiation of anaplastic thyroid carcinoma and accentuates radio-therapeutic response by regulating the Smad7-TGF-beta pathway. *Cell Death Differ* **27**, 497-508 (2020).

6. Laetitia G, Sven S, Fabrice J. Combinatorial Therapies in Thyroid Cancer: An Overview of Preclinical and Clinical Progresses. *Cells* **9**, (2020).

7. Hong CM, Ahn BC. Redifferentiation of Radioiodine Refractory Differentiated Thyroid

Cancer for Reapplication of I-131 Therapy. *Front Endocrinol (Lausanne)* **8**, 260 (2017).

8. Shen X, *et al.* Patient Age-Associated Mortality Risk Is Differentiated by BRAF V600E Status in Papillary Thyroid Cancer. **36**, 438-445 (2018).

9. Pozdeyev N, *et al.* Genetic Analysis of 779 Advanced Differentiated and Anaplastic Thyroid Cancers. **24**, 3059-3068 (2018).

10. Liu R, Bishop J, Zhu G, Zhang T, Ladenson P, Xing MJJo. Mortality Risk Stratification by Combining BRAF V600E and TERT Promoter Mutations in Papillary Thyroid Cancer: Genetic Duet of BRAF and TERT Promoter Mutations in Thyroid Cancer Mortality. **3**, 202-208 (2017).

11. Li Y, *et al.* CYP2S1 is a synthetic lethal target in BRAF-driven thyroid cancers. **5**, 191 (2020).

12. Tekpli X, *et al.* An independent poor-prognosis subtype of breast cancer defined by a distinct tumor immune microenvironment. *Nat Commun* **10**, 5499 (2019).

13. Roehlecke C, Schmidt MHH. Tunneling Nanotubes and Tumor Microtubes in Cancer. *Cancers (Basel)* **12**, (2020).

14. Oczko-Wojciechowska M, *et al.* Impact of the Tumor Microenvironment on the Gene Expression Profile in Papillary Thyroid Cancer. *Pathobiology* **87**, 143-154 (2020).

15. Jolly LA, *et al.* Fibroblast-Mediated Collagen Remodeling Within the Tumor Microenvironment Facilitates Progression of Thyroid Cancers Driven by BrafV600E and Pten Loss. *Cancer Res* **76**, 1804-1813 (2016).

16. Robertson A, *et al.* Identification of Differential Tumor Subtypes of T1 Bladder Cancer. **78**, 533-537 (2020).

17. Mer A, *et al.* Biological and therapeutic implications of a unique subtype of NPM1 mutated AML. **12**, 1054 (2021).

18. Job S, *et al.* Identification of Four Immune Subtypes Characterized by Distinct Composition and Functions of Tumor Microenvironment in Intrahepatic Cholangiocarcinoma. **72**, 965-981 (2020).

19. Wright G, *et al.* A Probabilistic Classification Tool for Genetic Subtypes of Diffuse Large B Cell Lymphoma with Therapeutic Implications. **37**, 551-568.e514 (2020).

20. Guruprasad P, Lee Y, Kim K, Ruella MJTJoem. The current landscape of single-cell

transcriptomics for cancer immunotherapy. **218**, (2021).

21. Lin W*, et al.* Single-cell transcriptome analysis of tumor and stromal compartments of pancreatic ductal adenocarcinoma primary tumors and metastatic lesions. *Genome Med* **12**, 80 (2020).

22. Stoeckius M*, et al.* Simultaneous epitope and transcriptome measurement in single cells. **14**, 865-868 (2017).

23. Butler A, Hoffman P, Smibert P, Papalexi E, Satija RJNb. Integrating single-cell transcriptomic data across different conditions, technologies, and species. **36**, 411-420 (2018).

24. Jerby-Arnon L*, et al.* A Cancer Cell Program Promotes T Cell Exclusion and Resistance to Checkpoint Blockade. **175**, 984-997.e924 (2018).

25. Peng J*, et al.* Single-cell RNA-seq highlights intra-tumoral heterogeneity and malignant progression in pancreatic ductal adenocarcinoma. **29**, 725-738 (2019).

26. Zhang X*, et al.* CellMarker: a manually curated resource of cell markers in human and mouse. **47**, D721-D728 (2019).

552 27. Zilionis R*, et al.* Single-Cell Transcriptomics of Human and Mouse Lung Cancers
553 Reveals Conserved Myeloid Populations across Individuals and Species. **50**,
554 1317-1334.e1310 (2019).
555
556 28. Luoma A*, et al.* Molecular Pathways of Colon Inflammation Induced by Cancer
557 Immunotherapy. **182**, 655-671.e622 (2020).
558
559 29. Habib N*, et al.* Disease-associated astrocytes in Alzheimer's disease and aging. *Nat*
560 *Neurosci* **23**, 701-706 (2020).
561
562 30. Steen CB, Liu CL, Alizadeh AA, Newman AM. Profiling Cell Type Abundance and
563 Expression in Bulk Tissues with CIBERSORTx. *Methods Mol Biol* **2117**, 135-157
564 (2020).
565
566 31. Hänzelmann S, Castelo R, Guinney JJBb. GSVA: gene set variation analysis for
567 microarray and RNA-seq data. **14**, 7 (2013).
568
569 32. Aibar S*, et al.* SCENIC: single-cell regulatory network inference and clustering. **14**,
570 1083-1086 (2017).
571
572 33. Efremova M, Vento-Tormo M, Teichmann S, Vento-Tormo RJNp. CellPhoneDB:
573 inferring cell-cell communication from combined expression of multi-subunit

574 ligand-receptor complexes. **15**, 1484-1506 (2020).

575

576 34. Trapnell C, *et al.* The dynamics and regulators of cell fate decisions are revealed by

577 pseudotemporal ordering of single cells. *Nat Biotechnol* **32**, 381-386 (2014).

578

579 35. Gao R, *et al.* Delineating copy number and clonal substructure in human tumors from

580 single-cell transcriptomes. *Nat Biotechnol*, (2021).

581

582 36. Wolford C, *et al.* Transcription factor ATF3 links host adaptive response to breast

583 cancer metastasis. **123**, 2893-2906 (2013).

584

585 37. Pere H, *et al.* A CCR4 antagonist combined with vaccines induces antigen-specific

586 CD8+ T cells and tumor immunity against self antigens. **118**, 4853-4862 (2011).

587

588 38. Berlato C, *et al.* A CCR4 antagonist reverses the tumor-promoting microenvironment

589 of renal cancer. **127**, 801-813 (2017).

590

591 39. Vinci M, *et al.* Functional diversity and cooperativity between subclonal populations of

592 pediatric glioblastoma and diffuse intrinsic pontine glioma cells. *Nat Med* **24**,

593 1204-1215 (2018).

594

595 40. Rubio-Perez C, *et al.* Immune cell profiling of the cerebrospinal fluid enables the

596 characterization of the brain metastasis microenvironment. **12**, 1503 (2021).

597

598 41. Chen YP*, et al.* Single-cell transcriptomics reveals regulators underlying immune cell
599 diversity and immune subtypes associated with prognosis in nasopharyngeal
600 carcinoma. *Cell Res* **30**, 1024-1042 (2020).

601

602 42. Cook PJ*, et al.* Cox-2-derived PGE2 induces Id1-dependent radiation resistance and
603 self-renewal in experimental glioblastoma. *Neuro Oncol* **18**, 1379-1389 (2016).

604

605 43. Jin S, Borkhuu O, Bao W, Yang YT. Signaling Pathways in Thyroid Cancer and Their
606 Therapeutic Implications. *J Clin Med Res* **8**, 284-296 (2016).

607

608 44. Yu J, Baron V, Mercola D, Mustelin T, Adamson ED. A network of p73, p53 and Egr1
609 is required for efficient apoptosis in tumor cells. *Cell Death Differ* **14**, 436-446 (2007).

610

611 45. Jung SN*, et al.* EGR1/GADD45alpha Activation by ROS of Non-Thermal Plasma
612 Mediates Cell Death in Thyroid Carcinoma. *Cancers (Basel)* **13**, (2021).

613

614 46. Crawford NT, McIntyre AJ, McCormick A, D'Costa ZC, Buckley NE, Mullan PB. TBX2
615 interacts with heterochromatin protein 1 to recruit a novel repression complex to
616 EGR1-targeted promoters to drive the proliferation of breast cancer cells. *Oncogene*
617 **38**, 5971-5986 (2019).

47. Ryu JW, *et al.* Paradoxical induction of growth arrest and apoptosis by EGF via the up-regulation of PTEN by activating Redox factor-1/Egr-1 in human lung cancer cells. *Oncotarget* **8**, 4181-4195 (2017).

48. Peng WX, *et al.* Egr-1 regulates irradiation-induced autophagy through Atg4B to promote radioresistance in hepatocellular carcinoma cells. *Oncogenesis* **6**, e292 (2017).

49. Gonzalez-Navajas JM, *et al.* The Impact of Tregs on the Anticancer Immunity and the Efficacy of Immune Checkpoint Inhibitor Therapies. *Front Immunol* **12**, 625783 (2021).

50. Antonelli A, Ferrari SM, Fallahi P. Current and future immunotherapies for thyroid cancer. *Expert Rev Anticancer Ther* **18**, 149-159 (2018).

51. Lv M, *et al.* Manganese is critical for antitumor immune responses via cGAS-STING and improves the efficacy of clinical immunotherapy. *Cell Res* **30**, 966-979 (2020).

52. Marigo I, *et al.* T Cell Cancer Therapy Requires CD40-CD40L Activation of Tumor Necrosis Factor and Inducible Nitric-Oxide-Synthase-Producing Dendritic Cells. *Cancer Cell* **30**, 377-390 (2016).

53. Cortez MA, *et al.* Bone morphogenetic protein 7 promotes resistance to immunotherapy. *Nat Commun* **11**, 4840 (2020).

54. Huang Z, *et al.* IL-27 promotes the expansion of self-renewing CD8(+) T cells in persistent viral infection. *J Exp Med* **216**, 1791-1808 (2019).

55. Lei Q, Wang D, Sun K, Wang L, Zhang Y. Resistance Mechanisms of Anti-PD1/PDL1 Therapy in Solid Tumors. *Front Cell Dev Biol* **8**, 672 (2020).

56. Severson JJ, *et al.* PD-1+Tim-3+ CD8+ T Lymphocytes Display Varied Degrees of Functional Exhaustion in Patients with Regionally Metastatic Differentiated Thyroid Cancer. *Cancer Immunol Res* **3**, 620-630 (2015).

57. Tirosh I, *et al.* Dissecting the multicellular ecosystem of metastatic melanoma by single-cell RNA-seq. **352**, 189-196 (2016).

58. Liu Y, Cao X. Characteristics and Significance of the Pre-metastatic Niche. *Cancer Cell* **30**, 668-681 (2016).

Acknowledgments

This work was supported by Shanghai Municipal Commission of Health and Family Planning Commission (2019SY062).

Authors' contributions

BH J, ZS W, ZQ Y, and Y R conceived and designed the study. WL J, CG T, and ZS W contributed to carry out the experiments. BH J, CG H, and C Y contributed to data analysis. ZS W, BH J, and ZQ Y wrote the manuscript. YR, WL J, and ZQ Y revised the paper. All authors read and approved the final manuscript.

Competing Interests

The authors have declared that no competing interest exists.

Figure legends

Fig.1 Overall design and single cell atlas in papillary thyroid carcinoma. a Workflow diagram showing the processing of samples. **b** UMAP plots of total cells, colored by the sample origin (tumor, metastatic LN, and paracancerous tissues). **c** Expression of cell marker genes. **d** Changes in frequency of multiple cell types and clusters in tumors and metastatic LNs. Asterisks on the left of the vertical line denote statistically significant differences between tumors and paracancerous tissues while asterisks on the right are used to show statistically significant differences between metastatic LNs and tumors. *$p < 0.05$, **$p < 0.01$, ***$p < 0.001$, two-tailed t-tests. **e** Interaction network constructed by CellPhoneDB. Size of circles and color of arrows represent interaction counts, and brighter color and larger size mean more interaction with other cell types.

Fig.2 Identification of malignant cells in epithelial cells. a Clonal substructure of epithelial cells delineated by clustering single-cell copy number profiles inferred from scRNA-seq data by CopyKAT. **b** UMAP plots of total epithelial cells, colored by the sample origin (left and middle). Cell counts of malignant and non-malignant cells, colored by the sample origin (right). **c** Differentiation trajectory of epithelial cells, with each color coded for pseudotime (right) and clusters (left). **d** Heatmap of the area under the curve (AUC) scores of transcription factor (TF) motifs estimated by SCENIC. Shown are differentially activated motifs in malignant and non-malignant cells, respectively. **e** High level of CREM and ETS1 predicted good prognosis in the TCGA THCA cohort. Log-rank p value < 0.05 was considered as statistically significant. **f** BHLHE40 was highly expressed in LN samples ($p < 0.001$). **g** GO enrichment analysis of up-regulated genes in malignant lymphatic metastasis cells.

Fig.3 Heterogeneity of T cell populations. a UMAP plot of T cells color-coded by their associated cell types. **b** Dotplot of cell markers; sizes of dots represent abundance while color represents expression level. **c** Potential new cell markers. **d** The protein level of EGR1 was decreased in tumor tissues compared with normal tissues. **e** High level of EGR1 predicted good prognosis in the TCGA THCA cohort. **f** Changes in frequency of multiple cell types in T cell populations. Asterisks on the left of the vertical line denote statistically significant differences between tumors and paracancerous tissues while asterisks on the right are used to show statistically significant differences between LNs and tumors. *$p < 0.05$, **$p < 0.01$, ***$p < 0.001$, two-tailed t-tests. **g** Violin of cell abundance predicted from the TCGA THCA cohort

by CIBERSORTx.

Fig.4 Novel cell type, named Protective EGR1^{+}CD4^{+} T cells, and potential therapeutic targets. a Differences in 50 hallmark pathway activities scored with GSVA software. Shown are t values calculated by a linear model. **b** Heatmap of the AUC scores of TF motifs estimated by SCENIC. Shown are differentially activated motifs in CD4^{+} Tregs and Protective EGR1^{+}CD4^{+} T cells, respectively. **c**-**d** Heatmap of positive and negative immune checkpoint expression on T cells in LNs (**c**) and tumors (**d**), respectively.

Fig.5 Heterogeneity of Myeloid cell populations. a UMAP plot of Myeloid cells color-coded by their associated cell types. **b** Dotplot of cell markers; sizes of dots represent abundance while color represents expression level. **c** Changes in frequency of multiple cell types and clusters in Myeloid cell populations. Asterisks on the left of the vertical line denote statistically significant differences between tumors and paracancerous tissues while asterisks on the right are used to show statistically significant differences between LNs and tumors. *$p < 0.05$, **$p < 0.01$, ***$p < 0.001$, two-tailed t-tests. **d** Violin of Macrophage abundance predicted from the TCGA THCA cohort by CIBERSORTx. **e** Kaplan-Meier curves of DFS based on the percentage of dendritic cells in the TCGA database.

Fig.6 M2 macrophages were strongly enriched in the tumor tissues. a-b Heatmap shows the differences in pathway activities scored by GSVA between different sample origins. Shown are t values calculated by a linear model. **c** Heatmap of the AUC scores of TF motifs estimated by SCENIC. Shown are differentially activated motifs in subtypes of Myeloid cells, respectively. **d** Violin plot shows the expression level of related genes in Macrophage subclusters (left) and cytokines in dendritic cells (right).

Supplementary information

Supplementary Fig. 1 Identification of major cell types in PTC. UMAP plots for expression of the marker genes from **Fig 1c** and of additional marker genes for major cell types. For B cells: CD19, MS4A1(CD20), CD38, CD79A, and CD79B; for CD4^{+} T cells: CD4 and CD3D; for CD8^{+}T cells: CD8A and CD3D; for Endothelial cells: CD34 and CD31(PECAM); for Epithelial cells: EPCAM and KRT18; for Fibroblasts: COL1A1; for Myeloid cells: CD14, CD86, ITGAX, CD80, CD83, and ITGAM; for Naive T cells: CCR7 and CD3D; for NKT cells: NKG7 and CD3D; for Plasma cells:

CD79A and SDC1.

Supplementary Fig. 2 Overview of the 28,205 single cells from tumors, paracancerous tissues, and metastatic LNs. a The fraction of multiple cell types originating from 7 tumor tissues, 6 paracancerous tissues, and 2 metastatic LNs. **b** The fraction of multiple cell types originating from 15 samples. **c** The number of multiple cell types. **d** Box plots of the number of transcripts.

Supplementary Fig. 3 Potential new cell markers in T cells.

Supplementary Fig. 4 DEGs related to $CD4^+$Tregs and transitional $EGR1^+CD4^+$T cells. a The expression of the maker genes in the TCGA THCA cohort. **b** Differences in 50 hallmark pathway activities scored with GSVA software. Shown are t values calculated by a linear model. **c** DEGs related to Protective $EGR1^+CD4^+$ T cells in tumors and LNs, respectively. **d** DEGs related to $CD4^+$Tregs in tumors and LNs, respectively. Upregulated genes and downregulated genes were colored in red and blue, respectively. FC≥2.

Supplementary Fig. 5 External verification based on the TCGA data. a High level of Macrophage abundance predicted poor prognosis in the TCGA THCA cohort, and neutrophil was the opposite. **b** Kaplan-Meier survival curve for IFITM2.

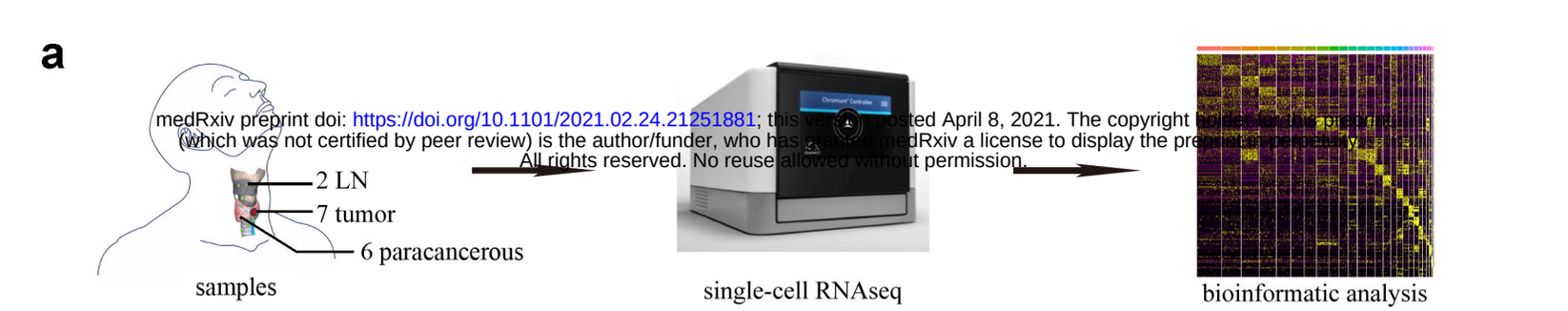

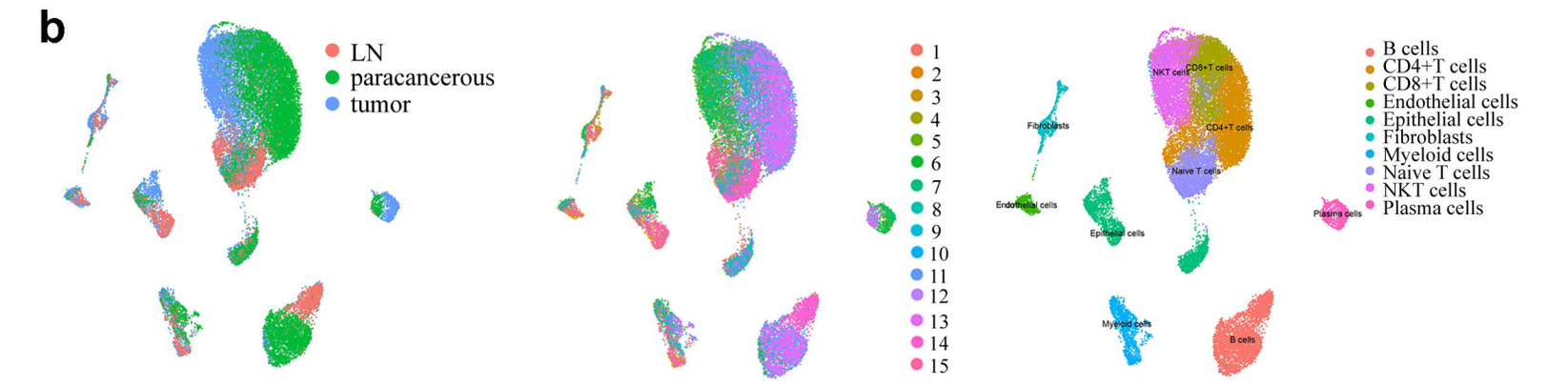

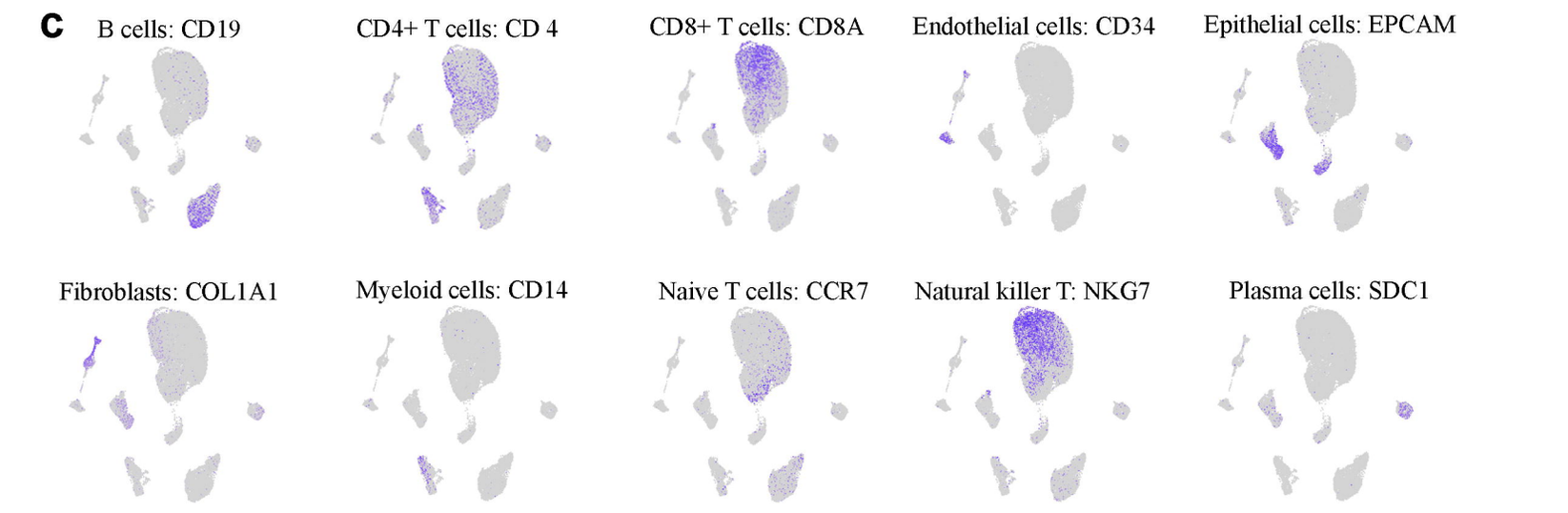

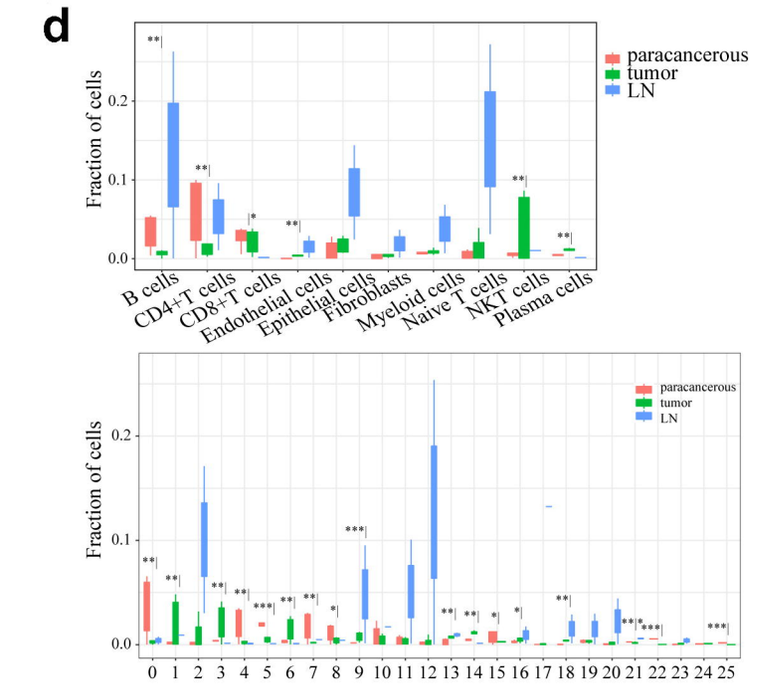

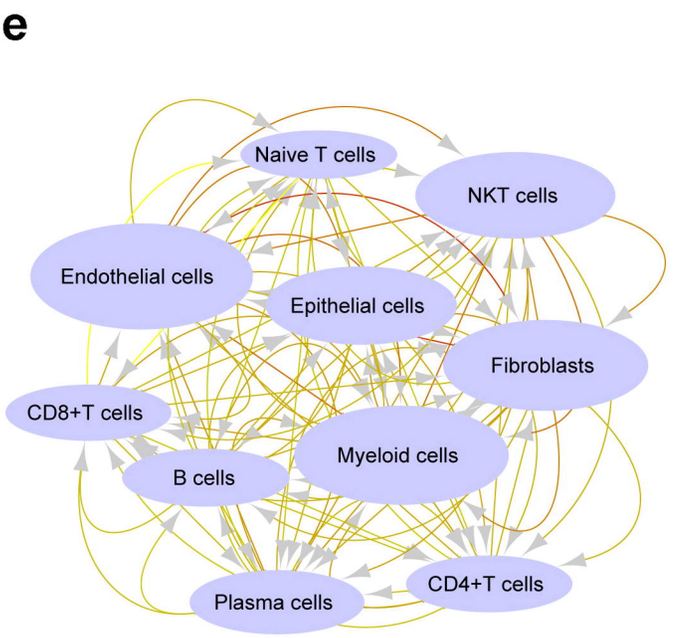

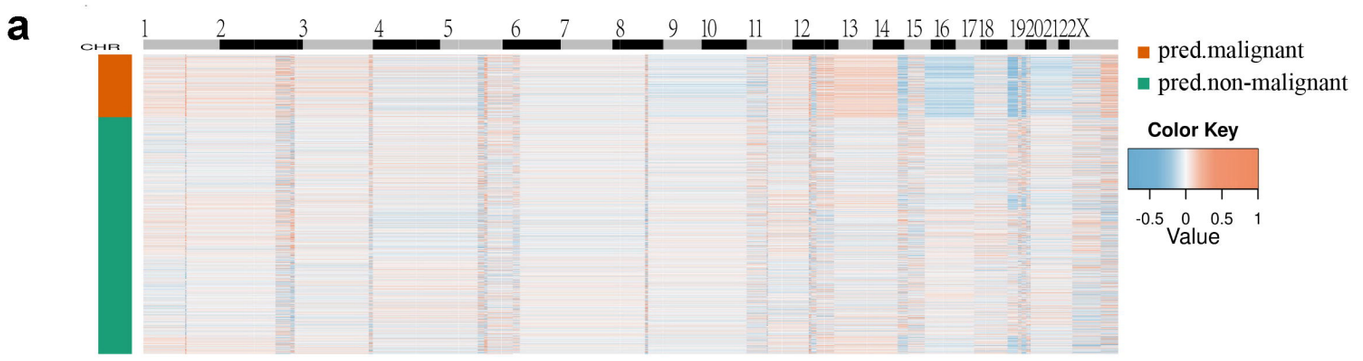

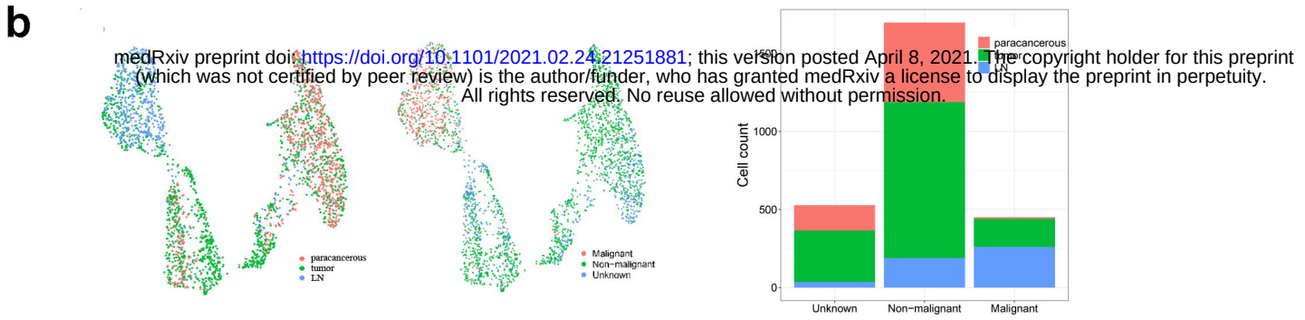

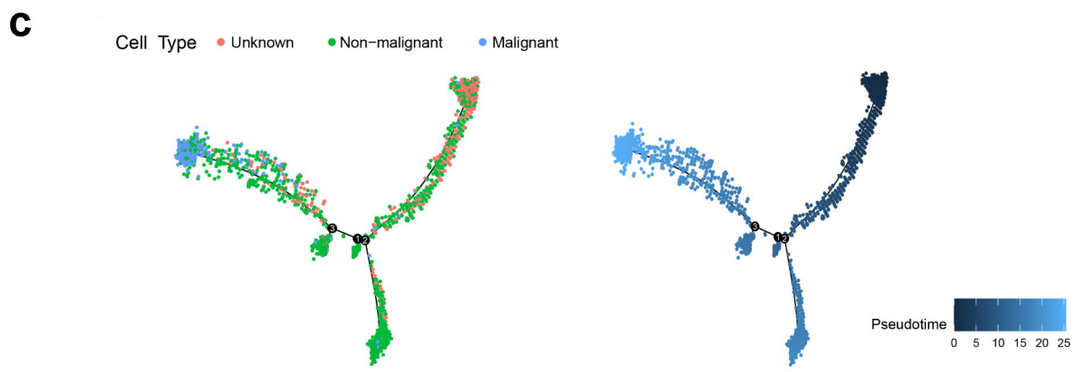

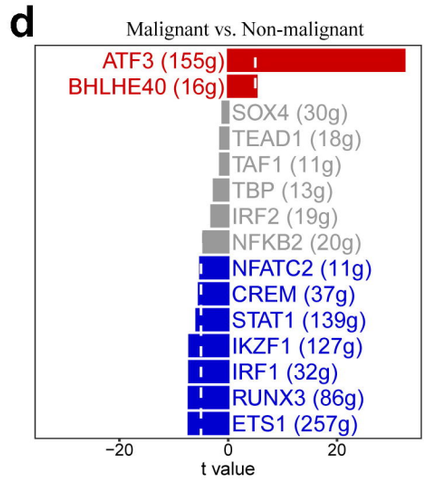

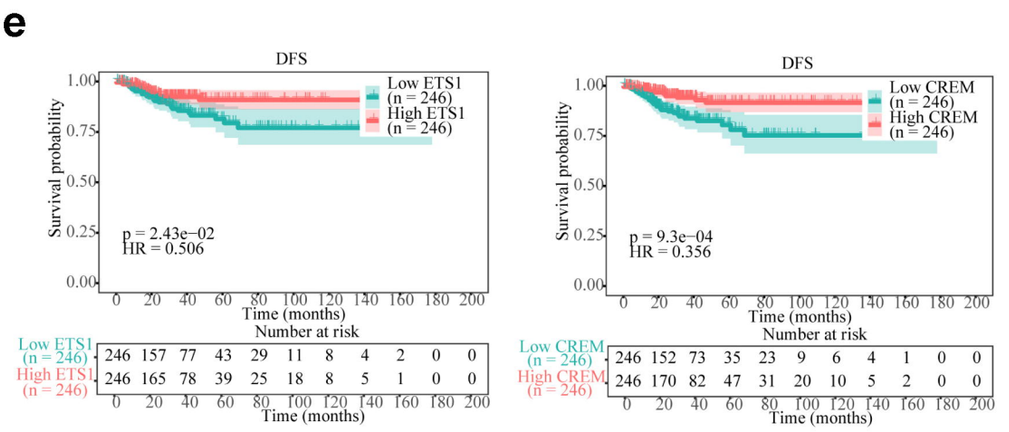

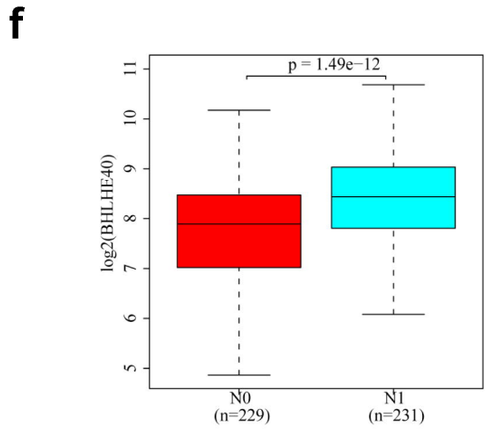

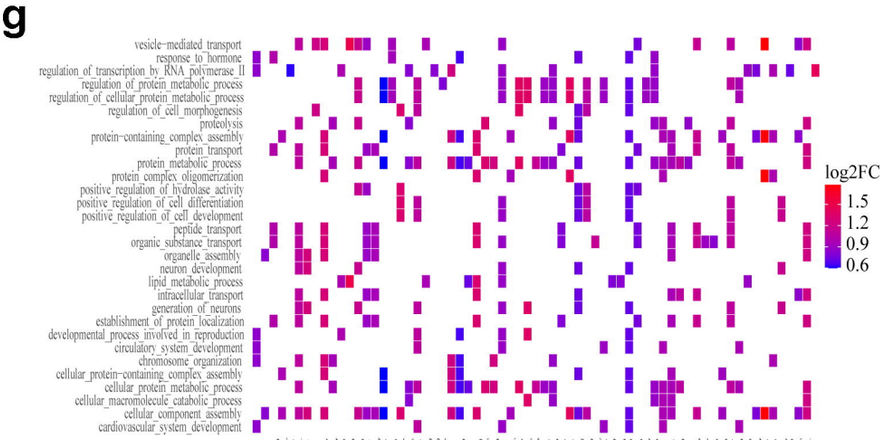

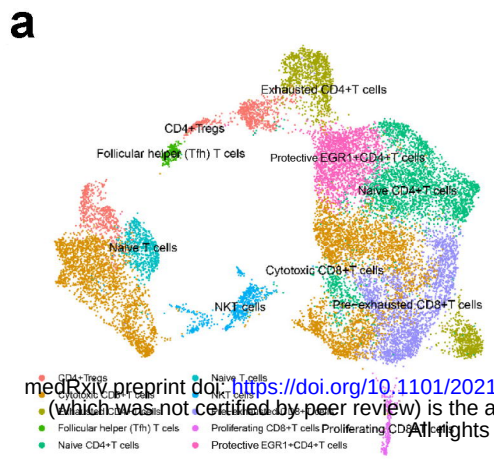

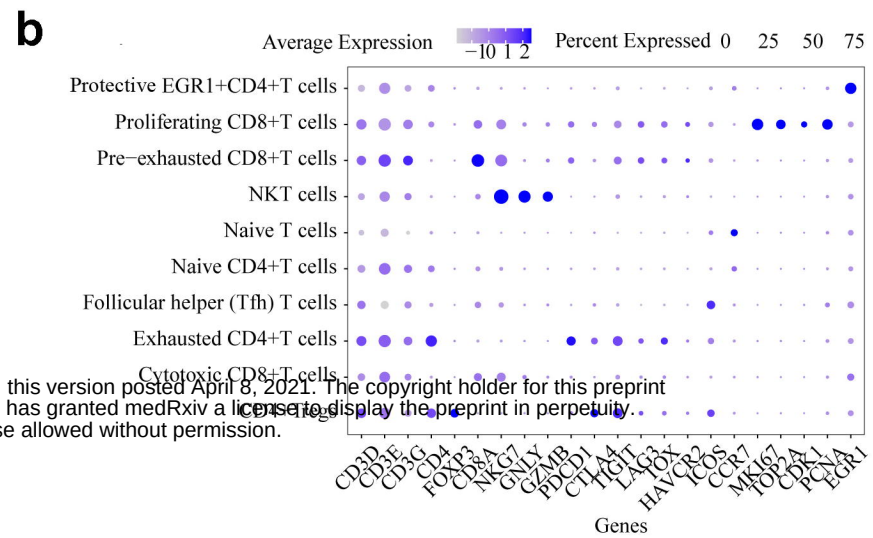

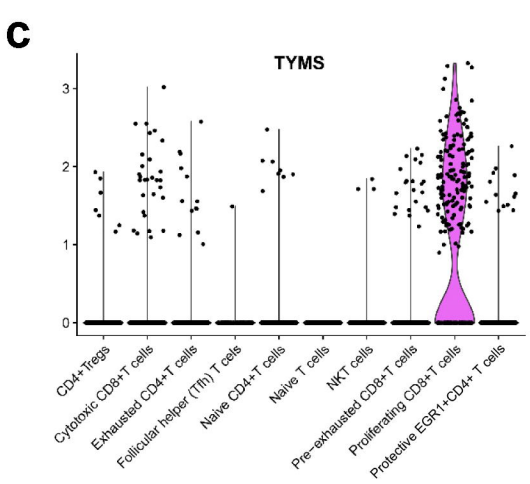

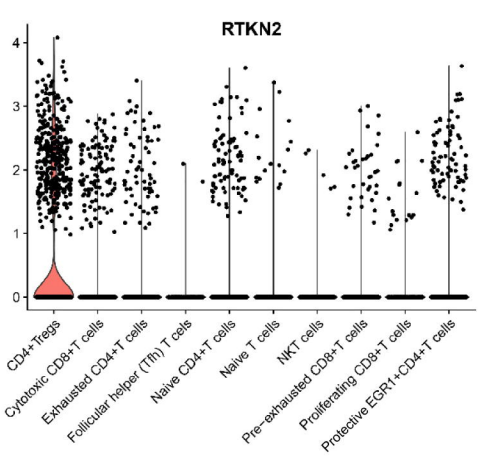

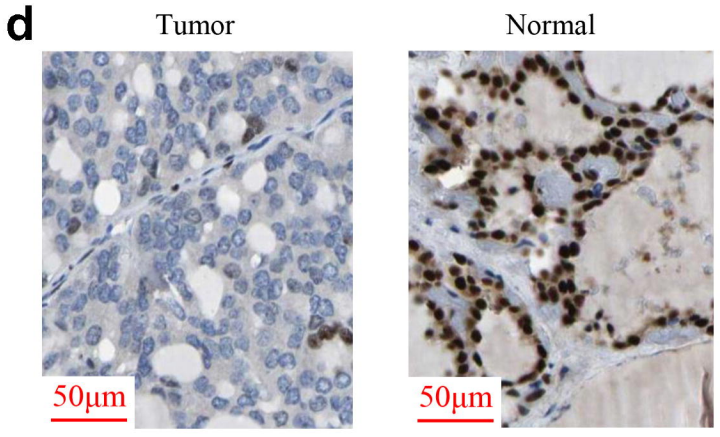

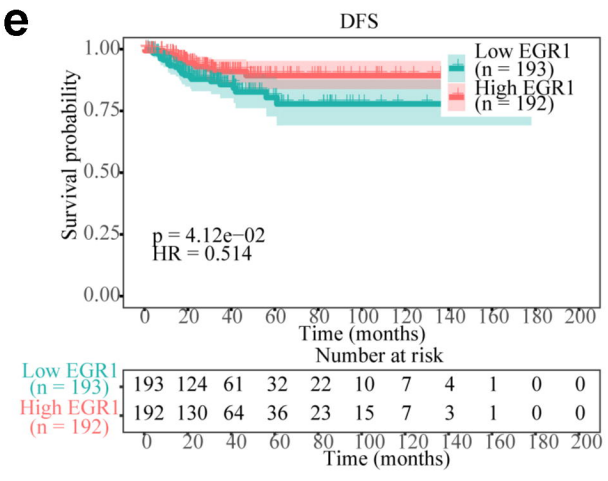

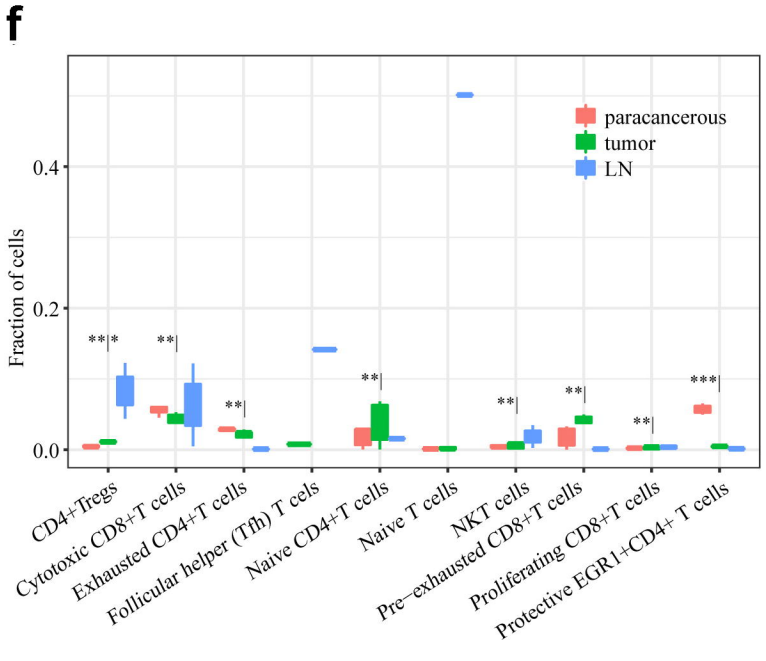

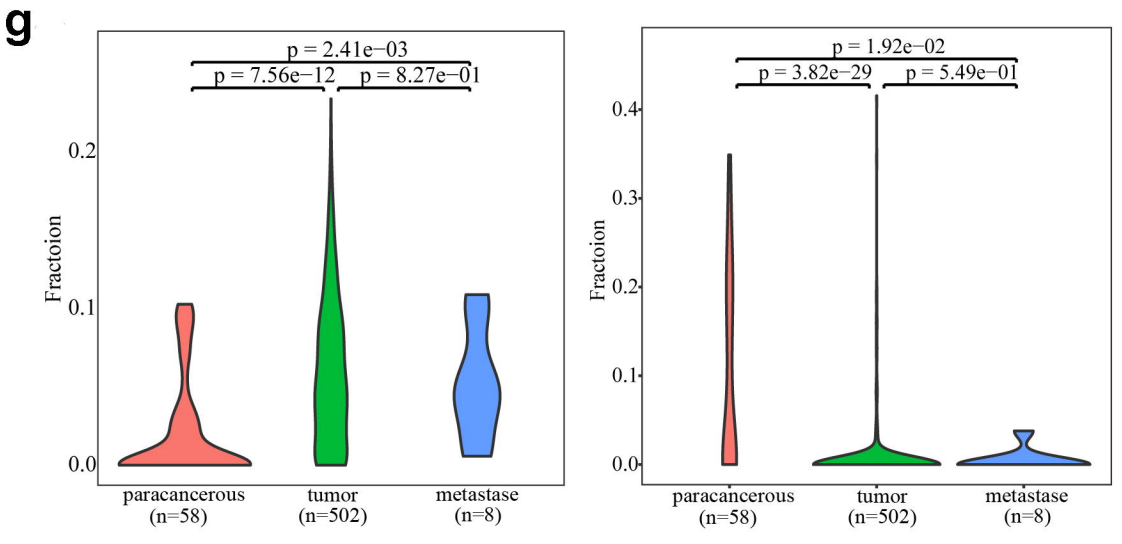

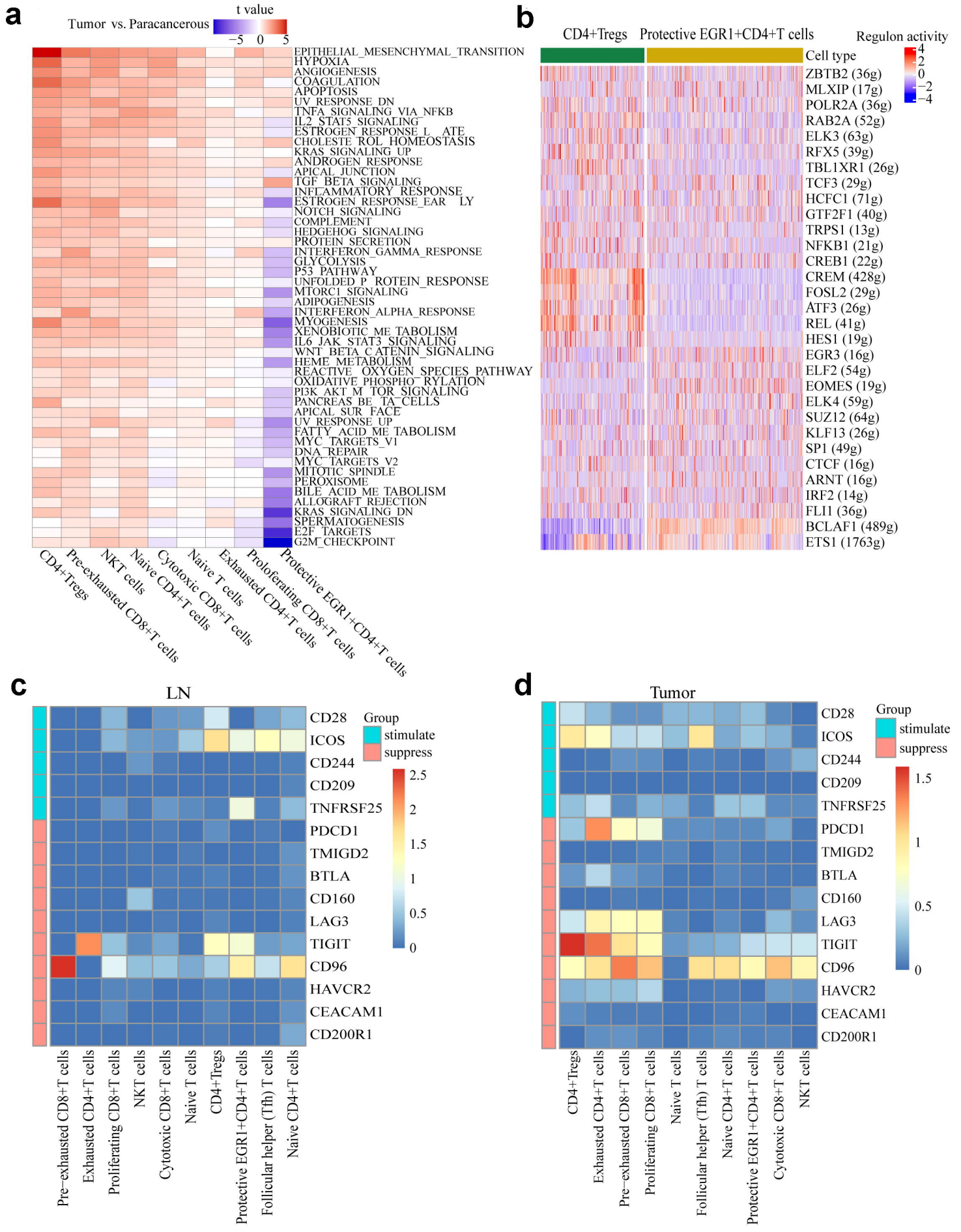
a
Tumor vs. Paracancerous
t value
−5 0 5
EPITHELIAL_MESENCHYMAL_TRANSITION
HYPOXIA
ANGIOGENESIS
COAGULATION
APOPTOSIS
UV_RESPONSE_DN
TNFA_SIGNALING_VIA_NFKB
IL2_STAT5_SIGNALING
ESTROGEN_RESPONSE_L ATE
CHOLESTE ROL_HOMEOSTASIS
KRAS_SIGNALING_UP
ANDROGEN_RESPONSE
APICAL_JUNCTION
TGF_BETA_SIGNALING
INFLAMMATORY_RESPONSE
ESTROGEN_RESPONSE_EAR LY
NOTCH_SIGNALING
COMPLEMENT
HEDGEHOG_SIGNALING
PROTEIN_SECRETION
INTERFERON_GAMMA_RESPONSE
GLYCOLYSIS
P53_PATHWAY
UNFOLDED_P ROTEIN_RESPONSE
MTORC1_SIGNALING
ADIPOGENESIS
INTERFERON_ALPHA_RESPONSE
MYOGENESIS
XENOBIOTIC_ME TABOLISM
IL6_JAK_STAT3_SIGNALING
WNT_BETA_C ATENIN_SIGNALING
HEME_METABOLISM
REACTIVE_OXYGEN_SPECIES_PATHWAY
OXIDATIVE_PHOSPHO RYLATION
PI3K_AKT_M TOR_SIGNALING
PANCREAS_BE TA_CELLS
APICAL_SUR FACE
UV_RESPONSE_UP
FATTY_ACID_ME TABOLISM
MYC_TARGETS_V1
DNA_REPAIR
MYC_TARGETS_V2
MITOTIC_SPINDLE
PEROXISOME
BILE_ACID_ME TABOLISM
ALLOGRAFT_REJECTION
KRAS_SIGNALING_DN
SPERMATOGENESIS
E2F_TARGETS
G2M_CHECKPOINT
CD4+Tregs
Pre-exhausted CD8+T cells
NKT cells
Naive CD4+T cells
Cytotoxic CD8+T cells
Naive T cells
Exhausted CD4+T cells
Proloferating CD8+T cells
Protective EGR1+CD4+T cells
b
CD4+Tregs
Protective EGR1+CD4+T cells
Regulon activity
4
2
0
−2
−4
Cell type
ZBTB2 (36g)
MLXIP (17g)
POLR2A (36g)
RAB2A (52g)
ELK3 (63g)
RFX5 (39g)
TBL1XR1 (26g)
TCF3 (29g)
HCFC1 (71g)
GTF2F1 (40g)
TRPS1 (13g)
NFKB1 (21g)
CREB1 (22g)
CREM (428g)
FOSL2 (29g)
ATF3 (26g)
REL (41g)
HES1 (19g)
EGR3 (16g)
ELF2 (54g)
EOMES (19g)
ELK4 (59g)
SUZ12 (64g)
KLF13 (26g)
SP1 (49g)
CTCF (16g)
ARNT (16g)
IRF2 (14g)
FLI1 (36g)
BCLAF1 (489g)
ETS1 (1763g)
c
LN
Group
stimulate
suppress
2.5
2
1.5
1
0.5
0
CD28
ICOS
CD244
CD209
TNFRSF25
PDCD1
TMIGD2
BTLA
CD160
LAG3
TIGIT
CD96
HAVCR2
CEACAM1
CD200R1
Pre−exhausted CD8+T cells
Exhausted CD4+T cells
Proliferating CD8+T cells
NKT cells
Cytotoxic CD8+T cells
Naive T cells
CD4+Tregs
Protective EGR1+CD4+T cells
Follicular helper (Tfh) T cells
Naive CD4+T cells
d
Tumor
Group
stimulate
suppress
1.5
1
0.5
0
CD28
ICOS
CD244
CD209
TNFRSF25
PDCD1
TMIGD2
BTLA
CD160
LAG3
TIGIT
CD96
HAVCR2
CEACAM1
CD200R1
CD4+Tregs
Exhausted CD4+T cells
Pre−exhausted CD8+T cells
Proliferating CD8+T cells
Naive T cells
Follicular helper (Tfh) T cells
Naive CD4+T cells
Protective EGR1+CD4+T cells
Cytotoxic CD8+T cells
NKT cells

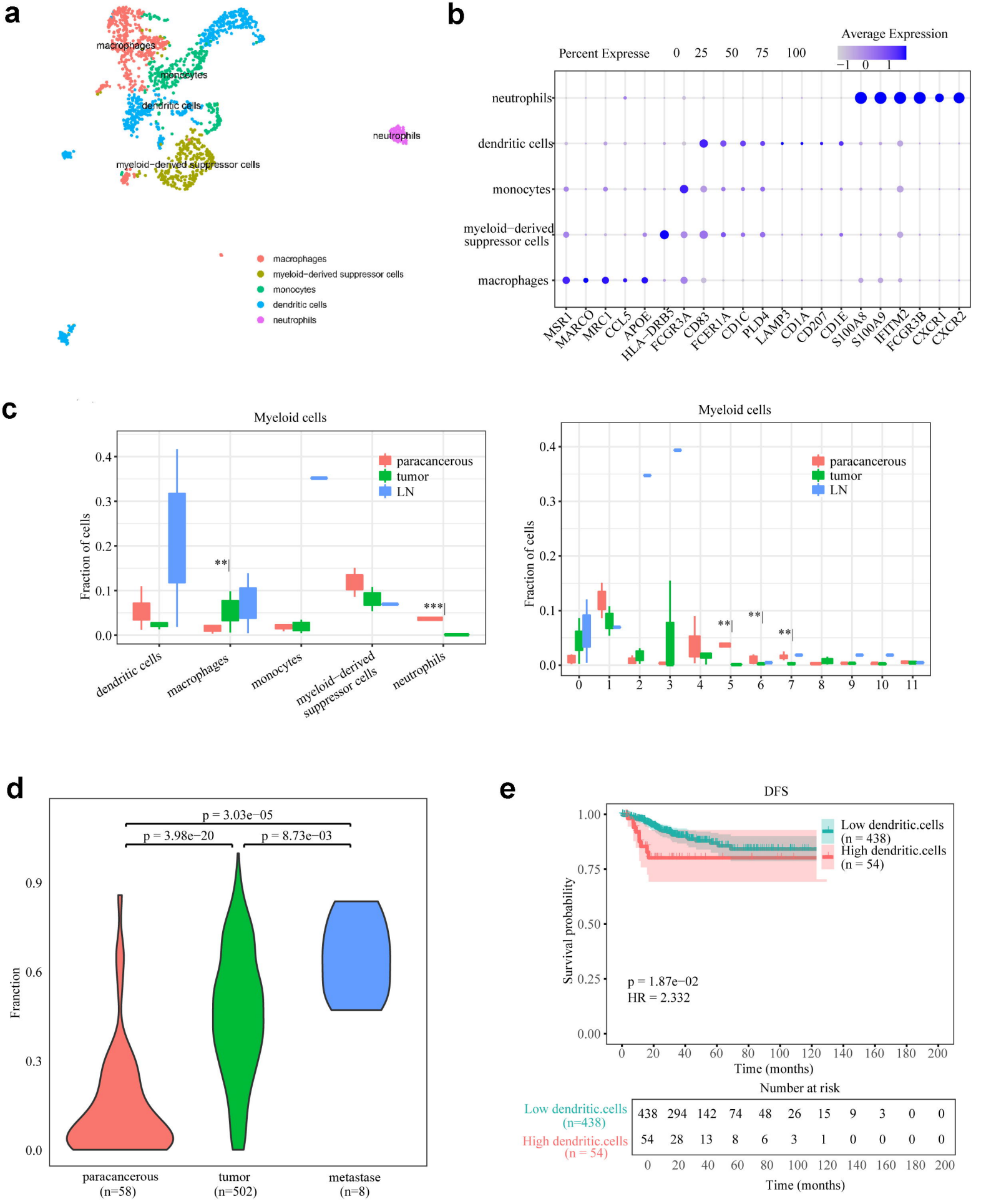
a
macrophages
monocytes
dendritic cells
neutrophils
myeloid−derived suppressor cells
macrophages
myeloid−derived suppressor cells
monocytes
dendritic cells
neutrophils
b
Percent Expresse
0
25
50
75
100
Average Expression
−1
0
1
neutrophils
dendritic cells
monocytes
myeloid−derived suppressor cells
macrophages
MSR1
MARCO
MRC1
CCL5
APOE
HLA−DRB5
FCGR3A
CD83
FCER1A
CD1C
PLD4
LAMP3
CD1A
CD207
CD1E
S100A8
S100A9
IFITM2
FCGR3B
CXCR1
CXCR2
c
Myeloid cells
Fraction of cells
paracancerous
tumor
LN
**
***
dendritic cells
macrophages
monocytes
myeloid−derived suppressor cells
neutrophils
Myeloid cells
Fraction of cells
paracancerous
tumor
LN
**
**
**
d
p = 3.03e−05
p = 3.98e−20
p = 8.73e−03
Franction
paracancerous (n=58)
tumor (n=502)
metastase (n=8)
e
DFS
Survival probability
Low dendritic.cells (n = 438)
High dendritic.cells (n = 54)
p = 1.87e−02
HR = 2.332
Time (months)
Number at risk
Low dendritic.cells (n=438)
438 294 142 74 48 26 15 9 3 0 0
High dendritic.cells (n = 54)
54 28 13 8 6 3 1 0 0 0 0
Time (months)